



RESEARCH

# Modelling of ductile fracture considering the effect of stress triaxiality and the energy partition theory in thin high-strength steel sheets

I. Tarhouni · P. Maimí · D. Frómeta · D. Casellas

Received: 22 June 2024 / Accepted: 17 February 2025  
© The Author(s) 2025

**Abstract** It is well recognized in the literature that the fracture process of thin metal sheets involves three energy dissipation mechanisms i.e., plasticity, necking and surface separation. However, the complex stress state in thin structures hinders the experimental assessment of these quantities and, consequently, the failure modelling. This work evaluates the contribution of these mechanisms to the ductile damage of a thin advanced high strength steel sheet under different stress triaxiality ranges. The essential work of fracture test was carried out on a set of different notch geometry specimens that cover a wide range of stress states. The experimental trend of these specimens was simulated in ABAQUS/Explicit using a VUSDFLD subroutine. Bai and Wierzbicki uncoupled fracture model, which is a function of fracture plastic strain to stress triaxiality ( $\eta$ ) and normalized Lode angle ( $\bar{\theta}$ ), was selected as damage initiation criterion. A quantitative relationship of the fracture energy ( $G_0$ ) as a

function of ( $\eta$ ) was proposed in this work and implemented in the model as a damage evolution law. The model captures well the experimental response and the influence of ( $\eta$ ) on the softening behavior of the material. It was found that the sensitivity of  $G_0$  to  $\eta$  is significant between 0.7 and 1.5. Above this range, it seems that ( $\eta$ ) has no influence on  $G_0$ . The model showed also the relationship between the two local damage parameters ( $G_0$ ) and the necking ( $G_n$ ) with respect to the stress state.  $G_0$  represents less than 10% of the total work of fracture, while the largest contribution comes from ( $G_n$ ).

**Keywords** Ductile damage · Complex-phase steel · Essential work of fracture · Fracture energy · Stress triaxiality · FEA

## List of symbols

$\bar{\epsilon}_p$	Equivalent plastic strain (dimensionless)
$\bar{\epsilon}_f$	Equivalent fracture strain (dimensionless)
$R$	Notch radius (m)
$\eta$	Stress triaxiality (dimensionless)
$\theta$	Lode angle (dimensionless)
$\bar{\theta}$	Normalized Lode angle (dimensionless)
$\bar{\sigma}$	Von Mises equivalent stress (Pa)
$r$	Third deviatoric stress invariant (Pa)
$\sigma_m$	Mean stress (Pa)
$\sigma_1, \sigma_2,$	Principal stresses (Pa)
$\sigma_3$	
$S$	Deviatoric stress tensor (Pa)

I. Tarhouni (✉) · D. Frómeta · D. Casellas  
Eurecat, Centre Tecnològic de Catalunya, Unit of Metallic and Ceramic Materials, Plaça de La Ciència, 2, 08243 Manresa, Spain  
e-mail: u1962647@campus.udg.edu

I. Tarhouni · P. Maimí  
AMADE, Polytechnic School, University of Girona, Campus Montilivi S/N, 17071 Girona, Spain

D. Casellas  
Division of Mechanics of Solid Materials, Luleå University of Technology, 971 87 Luleå, Sweden

$D$	Damage variable (dimensionless)
$DI$	Damage indicator for element deletion (dimensionless)
$W_f$	Total energy dissipated for fracture (J)
$w_f$	Total energy dissipated per unit area for fracture ( $J/m^2$ )
$W_p$	Energy dissipated due to plasticity (J)
$w_p$	Energy per unit volume dissipated due to plasticity ( $J/m^3$ )
$W_e$	Essential work of fracture (J)
$w_e$	Essential work of fracture per unit area ( $J/m^2$ )
$W_n$	Energy dissipated due to necking (J)
$G_n$	Energy per unit area dissipated due to necking ( $J/m^2$ )
$W_o$	Fracture energy dissipated due to material separation (J)
$G_o$	Fracture energy per unit area dissipated due to material separation ( $J/m^2$ )
$l$	Ligament length (m)
$l_E$	Characteristic length of a finite element (m)
$t$	Thickness of the test specimen (m)
$h$	Height of the localized plastic zone (m)
$L$	Length of the tensile specimen (m)
$f_t$	Tensile strength (Pa)
$\delta$	Crack opening (m)
$\delta_{co}$	Critical crack opening (m)
$A$	Cross section ( $m^2$ )
$a$	Crack length (m)

## 1 Introduction

Thin-walled metallic structures are used in the automotive industry to manufacture high performance parts. High strength materials are commonly applied to achieve vehicle lightweighting, among which Advanced High Strength Steels (AHSS) are the dominant ones to manufacture safety-related components.

The manufacturing process of these components involves hot and cold sheet forming processes that require plastically deforming the material beyond the yield strength. One of the important mechanisms characterizing the failure of thin metal structures is tensile flow localization or necking followed by a ductile fracture. Therefore, several theoretical and

numerical models have been developed over the years to predict accurately their failure while considering their characteristics, such as stable crack propagation prior to final fracture and large plastic zone ahead of the crack tip. Recently, the crack propagation resistance measured in the frame of fracture mechanics, i.e. the fracture toughness, has been postulated as a good descriptor of fracture resistance and crashworthiness (Frómet, et al. 2017).

Complex-phase (CP) steels belong to the first generation of AHSS family and show an excellent combination of strength and fracture toughness. Their yield strength and ultimate strength could range between 600 and 1000 MPa and between 800 and 1200 MPa, respectively, while showing high fracture toughness (more than  $250 \text{ kJ/m}^2$ ) and maintaining good ductility (7–15%) (Hilditch et al. 2015). Thanks to such outstanding properties combination, CP steels are mostly applied to manufacture parts requiring high fracture resistance, as components exposed to edge cracking during sheet manufacturing, or safety-related parts that require high energy absorption during crash events, such as sills, bumper brackets, impact beams etc., (Frómeta et al. 2017). Accordingly, the fracture resistance and damage mechanisms should be well understood to develop new steel grades, and to model the crash performance of thin-walled automotive parts.

Damage mechanisms controlling ductile fracture in structural metals at a micro-scale have been explored by several researchers in the past decade through micromechanical studies. It was found that microvoids nucleation, growth and coalescence is the major process controlling the local ductility and eventually leading to failure (Van Stone et al. 1985; Garrison and Moody 1987; Pardoen and Hutchinson 2000; Zhu et al. 2018; Koplík and Needleman 1988; Gao et al. 2005). Stiffness degradation and strain softening results in progressive damage involving nucleation and growth of microscopic voids, prior to final rupture by voids coalescence. The flow curve can be obtained by uniaxial test up to diffuse necking due to uniform stress distribution at the cross-section. Beyond this point, the stress distribution is no longer uniform, and a high triaxiality stress state takes place.

Earlier studies by McClintock (1968) and Rice and Tracey (1969), on the role of the stress state on ductile fracture strain revealed the strong dependency of the growth of both long cylindrical voids and spherical

voids on the hydrostatic pressure. Hancock and Mackenzie (1976) conducted experimental tests on notched round bar specimens covering a range of axisymmetric tension stress states. They reported that the strain to initiate fracture in a ductile solid correlates with the stress triaxiality. Hancock and Brown (1983) through plane strain and axisymmetric tensile specimens demonstrated that fracture strain is a decreasing function of triaxiality. Bao and Wierzbicki (2004, 2005) supported this argument through experimental and numerical results on different triaxiality regimes. However, they pointed out that the equivalent plastic strain to fracture is not a monotonic decaying function of triaxiality and presents some discontinuities, especially in low triaxialities.

More recent experimental and numerical studies showed that these models (accounting for triaxiality only) are not sufficient for the prediction of ductile fracture in low triaxiality and shear-dominated regimes (Xue 2007; Barsoum and Faleskog 2007; Kim et al. 2004). Later, it has been acknowledged that a new parameter needs to be considered to predict accurately the failure in ductile metals. This parameter is the Lode angle, which is related to the third invariant of the deviatoric stress tensor. Its influence can figure prominently in the coalescence of voids and stress carrying capacity of the material and, under constant triaxiality, the Lode angle is the dominant parameter controlling damage (Zhang et al. 2001; Gao and Kim 2006; Gao et al. 2009; Barsoum and Faleskog 2011; Yu 2015; Ma et al. 2017; Srivastava and Needleman 2013).

Bai and Wierzbicki (2008) suggested a new plasticity model to predict the ductility, accounting for the stress triaxiality and the lode angle simultaneously. Based on the classical plasticity theory, a 3D asymmetric failure surface considering the equivalent strain at fracture, stress triaxiality and Lode angle parameter was introduced. The calibration method of the fracture locus was also introduced and discussed in their work. Later, Bai and Wierzbicki (2009) proposed the Modified Mohr Coulomb criterion (MMC). Their model combined the Mohr–Coulomb model used in geomaterials with a new hardening model considering the pressure and Lode angle. The new model has been applied successfully in many studies to predict crack initiation and its direction (Dunand and Mohr 2011; Li et al. 2010; Sandin et al. 2021; Algarni 2015).

The energy dissipation mechanisms during a fracture process have been a research topic for many years (Cotterell and Reddel 1977; Hosford and Atkins 1990; Mai and Powell 1991; Tvergaard and Hutchinson 1992; Mai 1993; Pardoen et al. 2004). The total energy dissipated during a fracture process can be split into one part developed in the volume of the material ahead of the crack, due to plasticity, and another part spent in the fracture process zone (FPZ), due to damage and material separation. The Essential Work of Fracture (EWF) approach, first introduced by Cotterell and Reddel (1977), is one of the most effective and easy test methods used for the energy partition in metallic materials, following:  $W_f = W_p + W_e$ , where  $W_f$  is the total work,  $W_p$  is the plastic contribution, and  $W_e$  is the essential work of fracture. For a given thickness ( $t$ ),  $W_e$  is proportional to the fracture area, so the ligament length ( $l$ ), and  $W_p$  is proportional to the volume of the plastic zone, thus ( $l^2$ ). Therefore, the energy equation can be written as follows:  $W_f = w_e t l + \beta w_p t l^2$ , where  $w_p$  is the plastic work per unit volume of the plastic zone,  $w_e$  is the essential work per unit area of crack advance and  $\beta$  is a shape factor. In ductile fracture with extensive plastic deformation,  $W_e$  also is the contribution of two dissipation mechanisms: necking and material separation ( $W_n + W_o$ ), where  $W_n$  is thickness dependent (Pardoen et al. 2004).

Modelling of ductile fracture of AHSS has to consider the above-mentioned aspects to properly estimate the sheet fracture behavior during manufacturing and crash performance of structural automotive components. Accordingly, this work investigates the ductile fracture behavior of a new generation of CP steels with enhanced formability through an experimental–numerical study. Fracture mechanics tests under different stress states were conducted using notched specimens, with four notch radii values, including a pre-cracked condition, to cover different ranges of stress triaxiality. The MMC ductile fracture criterion and a quantitative relationship between the fracture energy and the triaxiality postulated in this work were used to model crack initiation and propagation. The material model was implemented in ABAQUS/Explicit using USDFLD subroutine. The predictive capability of the model, as well as a discussion on the energy partitioning, during the fracture process of this material, are presented herein.

## 2 Material characterization and experimental procedure

### 2.1 Material characterization

The studied AHSS is a new generation of CP steel, named CP1000HD, characterized by improved forming properties, high yield strength, high resistance to edge cracking and high crash energy absorption. The sheet thickness is 1.5 mm. The plastic strain- true stress behavior of CP1000HD (Fig. 1) was obtained using a Stiebler plastic hardening model (Stiebler et al. 1991) (Eq. 1). An inverse modelling approach was used to calibrate the materials parameters by fitting the force–elongation of a FE model of a tensile specimen (R3.75) to the experimental one. The calibration procedures are detailed in (Sandin et al. 2021).

$$\sigma(\varepsilon_p) = A + B\varepsilon_p + C(1 - \exp(-D\varepsilon_p)) \tag{1}$$

### 2.2 Stress state characterization and failure model calibration

The stress state in an isotropic solid material is conventionally defined by a 2nd order symmetric tensor  $[\sigma]$  and can be expressed in terms of three stress invariants ( $\sigma_m, \bar{\sigma}, r$ ) or the three principal stress  $\sigma_1 \geq \sigma_2 \geq \sigma_3$ .

$$\sigma_m = \frac{1}{3} tr(\sigma) \tag{2}$$

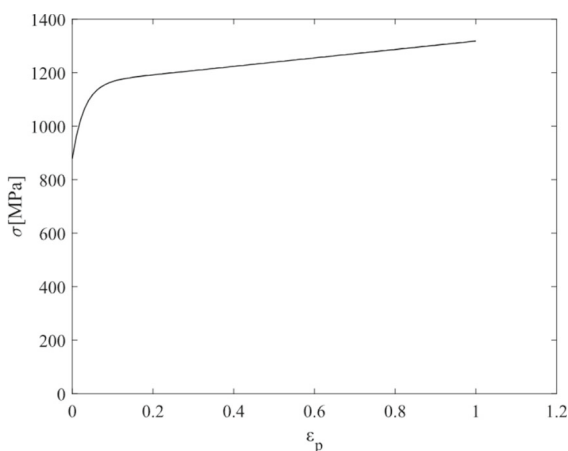


**Fig. 1** True stress–strain curves

$$\begin{aligned} \bar{\sigma} &= \sqrt{\frac{3}{2} S : S} \\ &= \sqrt{\frac{1}{2} [(\sigma_1 - \sigma_2)^2 + (\sigma_2 - \sigma_3)^2 + (\sigma_3 - \sigma_1)^2]} \end{aligned} \tag{3}$$

$$\begin{aligned} r &= \left[ \frac{27}{2} \det([S]) \right]^{1/3} \\ &= \left[ \frac{27}{2} (\sigma_1 - \sigma_m)(\sigma_2 - \sigma_m)(\sigma_3 - \sigma_m) \right]^{1/3} \end{aligned} \tag{4}$$

where  $\sigma_m$  is the hydrostatic pressure,  $[S] = [\sigma] - \sigma_m [I]$  is the deviatoric component of the stress tensor  $[\sigma]$ ,  $\bar{\sigma}$  is the Von Mises stress, and  $r$  is the third invariant of the deviatoric stress tensor  $[S]$ .

The prediction of ductile damage and fracture is receiving more and more attention in many sectors such as the automotive industry. However, the accurate prediction of failure especially in thin metal sheets, where high ductility is taking part, requires robust numerical models to account for all the material parameters involved in the failure mechanism. The MMC ductile fracture model, proposed by Bai and Wierzbicki (2009), has been successfully applied to predict ductile fracture initiation. The hydrostatic pressure (expressed in terms of stress triaxiality,  $\eta$ ) and the third invariant of the deviatoric stress tensor related to the Lode angle parameter ( $\bar{\theta}$ ) were used as stress state parameters for the model. The MMC fracture criterion represents a 3D fracture envelop that describes the monotonic decrease of ductility as a function of the increase of triaxiality ( $\eta$ ) and the lode parameter ( $\bar{\theta}$ ) as follow:

$$\begin{aligned} \varepsilon_f(\eta, \bar{\theta}) &= \left\{ C_2 \left[ C_3 + \frac{\sqrt{3}}{2 - \sqrt{3}} (C^{ax} - C_3) \left( \sec\left(\frac{\bar{\theta}\pi}{6}\right) - 1 \right) \right] \right. \\ &\quad \left. \left[ \sqrt{\frac{1 + C_1^2}{3}} \cos\left(\frac{\bar{\theta}\pi}{6}\right) + C_1 \left( \eta + \frac{1}{3} \sin\left(\frac{\bar{\theta}\pi}{6}\right) \right) \right] \right\}^{-\frac{1}{C_5}} \end{aligned} \tag{5}$$

where:

$$C^{ax} = \begin{cases} 1 & \text{for } \bar{\theta} \geq 0 \\ C_4 & \text{for } \bar{\theta} < 0 \end{cases}$$

$\eta$  is the stress triaxiality,  $\bar{\theta}$  is the normalized lode angle, and  $C_1$  to  $C_5$  are the shape parameters that have to be calibrated from experimental tests. The stress triaxiality ( $\eta$ ) is the normalized pressure, defined as:

**Table 1** Specimens designation and triaxiality range

Specimen	R15	Central hole	R3.75	Shear
$\eta$ -range	0.4–0.5	0.33	0.5	0

$$\eta = \frac{\sigma_m}{\bar{\sigma}} \quad (6)$$

The Lode angle  $\theta$  can be defined by the normalized third invariant ( $r$ ) of the deviatoric stress tensor as follows:

$$\cos(3\theta) = \left(\frac{r}{\bar{\sigma}}\right)^3 \quad (7)$$

where  $\theta$  is the lode angle ( $0 \leq \theta \leq \frac{\pi}{3}$ ).

Therefore, the normalized Lode angle or the Lode angle parameter ( $-1 \leq \bar{\theta} \leq 1$ ) is defined as:

$$\bar{\theta} = 1 - \frac{6}{\pi}\theta \quad (8)$$

For a proportional loading, the fracture surface is an asymmetric function of ( $\bar{\theta}$ ).

In the study of Sandin et al. (2021), the stress state parameters ( $\eta$ ,  $\bar{\theta}$ ) for CP1000HD were calibrated through experimental tests on four flat tensile test specimens with different geometries that cover a large range of stress states (Table 1). The first two types of specimens are dogbone specimens designated R15 and R3.75 with a notch of 15 mm and 3.75 mm radii respectively and a gauge width of 7.5 mm. The flat central hole specimen has a hole of 7.5 mm diameter at the center with a gauge length of 15 mm and finally a pure-shear specimen. All the test coupons were machined perpendicular to the rolling direction of the metal sheet.

Digital Image Correlation (DIC) and stepwise modelling method by Marth et al. (2016) were used to obtain the equivalent fracture strain ( $\epsilon_f$ ) and the stress triaxiality ( $\eta$ ) from the four tensile test specimens. With this data, it was possible to calibrate the MMC fracture locus for CP1000HD in Fig. 2 according to Bai and Wierzbicki (2009). The same curve was used as input for this study, with an extension to a high range of stress triaxiality up to 3 due to the high ductility of the material (Fig. 2).

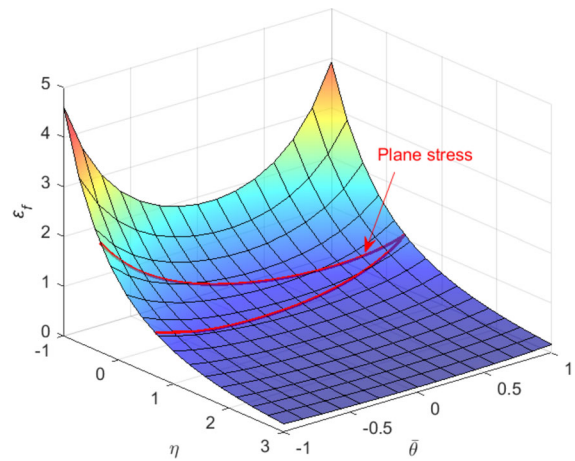


**Fig. 2** Modified Mohr–Coulomb fracture surface for the investigated materials. The red curve represents the plane stress state

### 2.3 Fracture toughness assessment

The fracture toughness of CP1000HD was assessed using the essential work of fracture (EWF) methodology. Double-edge notched tension (DENT) specimens with 200 mm long ( $L$ ), 55 mm wide ( $W$ ) and 1.5 mm thick ( $t$ ) were machined perpendicular to the rolling direction of the same metal sheet (Fig. 3). The test was conducted on four batches of specimens with the same dimensions but different notch radii. Four notch radius sizes of 150  $\mu\text{m}$ , 250  $\mu\text{m}$ , 500  $\mu\text{m}$  and 0.1  $\mu\text{m}$  (fatigue pre-crack) were chosen to cover different ranges of stress triaxiality. The first three types of notched specimens were machined by electrical discharge machining. The fourth size i.e., a crack tip has a radius of 0.1  $\mu\text{m}$ , was obtained by propagating a fatigue pre-crack of around 1 mm length from a notch root of 150  $\mu\text{m}$ . The specimens herein will be designated as NR150, NR250 and NR500 for notch radii of 150, 250 and 500  $\mu\text{m}$  respectively, and FPC for the fatigue pre-cracked specimens. A ligament length ( $l$ ) varying between 6 and 14 mm was used for all the geometries, following the EWF procedure detailed in CWA 17793 (2021). For each ligament length, 2–3 specimens were tested to increase the precision of the experimental measurements. All the specimens were tested under a quasi-static loading rate of 1 mm/min. The displacement was measured directly on the surface of the specimens at an initial gauge length of 50 mm. An extensometer was used to measure the displacement on the surface of the

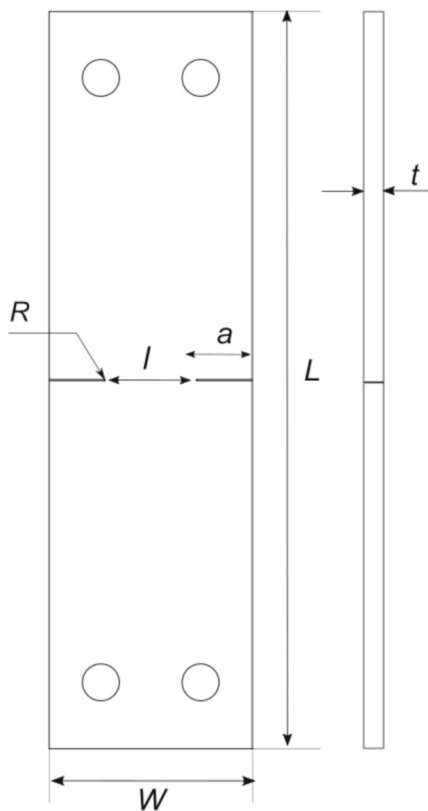


**Fig. 3** Geometry of the test specimens

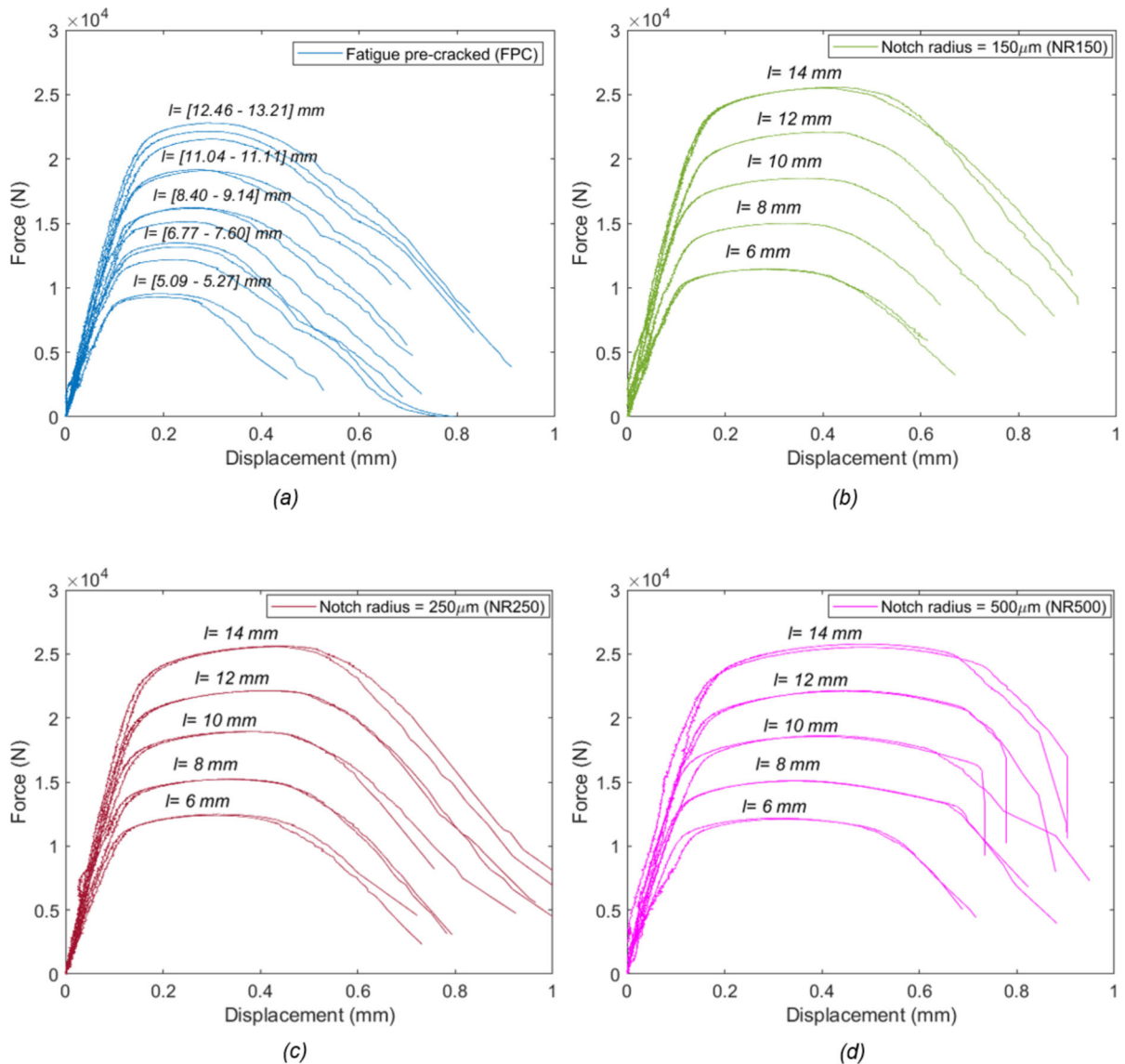
specimens during the loading from the elongation of an initial gauge length of 50 mm. A displacement control loading scheme was used to monitor the crack growth until the complete fracture of the test specimen.

Figure 4 shows the experimental force–displacement curves obtained from the EWF tests. It is obvious that all the test specimens of the same ligament length reached approximately the same maximum applied load, independently of the notch radius, except for FPC specimens. This difference in the maximum load capacity between FPC specimens and the other notch radii comes from the mismatch in the ligament lengths, as it is difficult to obtain the exact desired ligament length by fatigue pre-cracking. The force–displacement curves of NR150, NR250 and NR500 specimens display a long yield plateau, associated with the generation of a necking crack. The length of such plateau is higher for a larger notch radius. On the other hand, a shorter yield platform can be distinguished from the force displacement of FPC specimens, especially at large ligament lengths, because the

high triaxiality at the crack-tip reduces the amount of necking that can be developed. Besides the length of the platform, the onset of damage and softening as well, significantly depends on the notch radius. The increase of the notch radius delays damage and fracture initiation. For instance, material softening and degradation initiates at approximately 0.25–0.4 mm for FPC, 0.4–0.5 mm for NR150 and NR250 and 0.55–0.7 mm for NR500, similar observation was also made by Omiya et al. (2022). After the onset of damage, it can be observed that FPC, NR150 and NR250 exhibit a monotonous stiffness degradation and softening until complete failure. Contrarily, NR500 shows a sudden drop in the load after a certain amount of stable crack advance, especially for larger ligament lengths.

The EWF results for the tested notch radii are plotted together in Fig. 5 Total work of fracture vs ligament length for DENT specimens with different notch radii. for comparison. As already reported by other authors (Vratnica 2010; Frómata et al. 2019a; Pluinage 2001; Kaufman 2001; Pluinage and Gilgert 2003) the fracture toughness of the material is highly influenced by the notch radius. A  $w_e = 304 \text{ kJ/m}^2$  was obtained by pre-cracked DENT specimens i.e., the FPC ones. This is considered as the *real* fracture toughness of the material, while the results with notched specimens include also global plasticity and the obtained value cannot be considered as the material fracture toughness. Accordingly, as the notch radius increased, the fracture resistance increased resulting in values of  $475 \text{ kJ/m}^2$ ,  $514 \text{ kJ/m}^2$  and  $606 \text{ kJ/m}^2$  for NR150, NR250 and NR500, respectively (see Table 2). It is also worth mentioning, that the plastic work,  $w_p$ , of all the tested geometries, except NR500 is nearly the same with  $w_p = 33 \text{ MJ/m}^3$  for FPC,  $w_p = 30 \text{ MJ/m}^3$  for NR150 and  $w_p$  equal to  $32 \text{ MJ/m}^3$  for NR250, as denoted by the parallel regression lines. On the other hand, the linear regression of NR500 specimens yielded a lower plastic work value ( $w_p = 23 \text{ MJ/m}^3$ ). Additionally, a discrepancy in the results of this notch radius can be clearly observed. The NR500 data points follow roughly a linear trend resulting in very low correlation coefficients ( $R^2 = 0.59$ ) compared to the other geometries with  $R^2$  equal to or above 0.9.

Pardoen et al. (2004) conducted a series of experimental tests on DENT specimens of different thin metal sheets of various thicknesses, aimed to separate



**Fig. 4** Force–displacement curves of the DENT specimens with different notch radii and ligament lengths ( $l$ ) of CP1000HD. **a** FPC; **b** NR150; **c** NR250; **d** NR500

the contribution of necking to the intrinsic energy related to crack tip fracture. According to his study, the energy dissipated in the fracture of thin metal sheets can be divided into three terms (Fig. 6). The first contribution comes from plasticity before necking. The plastic work scales with the crack advance and the size of the specimen. Therefore,  $W_p$  can be written as:

$$W_p = \int w_p dV \approx w_p LA \quad (9)$$

where  $L$  is proportional to the ligament length for the DENT geometry.

A typical response of a ductile metal subjected to uniaxial tension is represented in Fig. 6. Before the maximum load, the specimen goes through linear deformation, the straight-line region of the curve indicated by (A), followed by a plastic strain hardening (A-N). During this phase, the deformation is homogeneous and uniform all over the specimen.

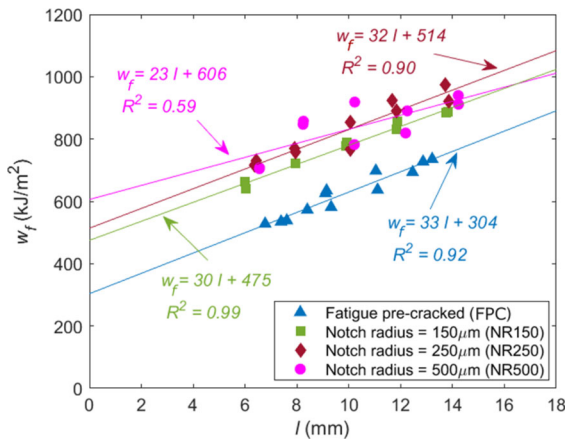


**Fig. 5** Total work of fracture vs ligament length for DENT specimens with different notch radii

**Table 2** Values of each energy dissipation mechanism for different notch root radii in the DENT

	FPC	NR150	NR250	NR500
$w_p$ [kJ/m <sup>3</sup> ]	33	30	32	23
$w_e$ [kJ/m <sup>2</sup> ]	304	475	514	606
$G_n$ [kJ/m <sup>2</sup> ]	294	445	474	556
$G_0$ [kJ/m <sup>2</sup> ]	10	30	40	50
$G_0/G_n$	0.034	0.067	0.084	0.089

$w_e$  specific essential work of fracture,  $w_p$  specific plastic work,  $G_n$  fracture energy associated to necking,  $G_0$  fracture energy associated to damage and material separation in the FPZ

The value of  $G_0$  was obtained numerically

After the maximum load, necking initiates (N) and deformation starts to localize in an approximately constant wide  $h$  region, that increases with specimen thickness. Consequently, the specimen elongates in the loading direction and contracts in the thickness direction. Thus, the negative slope of engineering stress–strain curve. The energy dissipation associated with localized necking scales with the thickness of the specimen as follow:

$$W_n = \int w_n dV_L \approx h \bar{w}_n A \approx G_n A \tag{10}$$

where  $G_n$  is the fracture energy associated with necking per unit area of crack advance. As the load continues to increase the deformation localizes in a narrower region and strain reaches very high values, this point is defined by  $DI = 1$  in Fig. 6 and, under

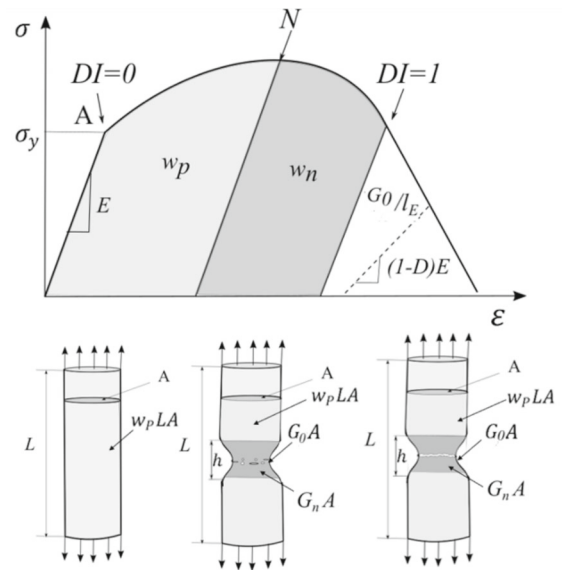


**Fig. 6** Schematic illustration of the energy partitioning during ductile fracture process

monotonic loading, corresponds to the strain defined by Eq. 5. Within this region, ductile degradation starts by growth and coalescence of voids until final fracture. The energy associated with the growth and coalescence of voids in a unit cell is expressed as:

$$W_0 = G_0 A \tag{11}$$

where  $G_0$  is the fracture energy per unit area of crack advance associated with the damage and material separation in the fracture process zone, and scales with the yield stress and the mean of voids spacing.

Accordingly, the energy dissipated in the fracture of ductile thin metal sheets can be divided into three terms:

$$W_f = W_p + W_n + W_0 = w_p LA + G_n A + G_0 A \tag{12}$$

$W_p$  scales with the volume of the plastic zone, whereas  $W_n$  and  $W_0$  scale with the cracked area, for instance, the ligament area in DENT specimens. In the EWF test,  $G_0 + G_n$  are obtained by extrapolating the regression line to a ligament length equal to zero (Fig. 5) and designated as  $w_e$  and expressed in [kJ/m<sup>2</sup>]. As stated in (Pardoen et al. 2004),  $G_n$  is usually larger than  $G_0$ , whereas  $w_p$  is the slope of the linear regression and is expressed in [MJ/m<sup>3</sup>]. The EWF equation is written as:

$$w_f = w_e + \beta w_p L \quad \text{where} \quad w_e = G_n + G_0 \tag{13}$$

The detailed description of the energy partitioning during the ductile fracture, illustrated in Fig. 6, will provide the foundation for the experimental–numerical correlation, which will be discussed in detail in Sect. 4.

### 3 Implementation of ductile damage model

#### 3.1 Finite element model

The numerical simulation was performed on the geometries considered in the experimental study using FE code ABAQUS/Explicit. A 3D solid element with reduced integration was used for all the models. Owing to the symmetry of the test specimens, only half of the specimens were modelled, and a symmetry condition was applied in the width direction following the x-axis (Fig. 7). A very fine and regular mesh was used in the ligament length zone where necking and fracture take place. The rest of the specimen was modelled with a coarse mesh. 8 elements were used through the thickness. To capture the stress singularity in the FPC specimens, the fatigue pre-cracks were modelled by removing a line of elements, that corresponds to the initial pre-crack lengths, from the mesh.

#### 3.2 Constitutive model

The model is based on  $J2$  (Von Mises) yield surface with an associated flow rule, a nonlinear isotropic hardening is defined following Eq. 1 and Fig. 1. Large deformation was considered through “NLGEOM” function to account for the necking. Additionally, a smeared cohesive law is used to account for the energy due to damage.

##### 3.2.1 Calibration of plasticity and ductile damage criterion

The true stress–strain curve in Fig. 1 was used as material input data for the model. The ductile damage criterion implemented in ABAQUS was used to reproduce the behavior of the material in this study. The onset of failure and progressive damage can be modelled by specifying a damage initiation criterion and damage evolution response. The ductile damage initiation criterion predicts the onset of damage due to nucleation, growth, and coalescence of microvoids in ductile metals and can be used in conjunction with Mises plasticity. The model assumes that the equivalent plastic strain at the onset of damage ( $\epsilon_f$ ) is a function of the stress triaxiality ( $\eta$ ). The dependency on the Lode angle ( $\bar{\theta}$ ) can also be introduced in the Explicit solver.

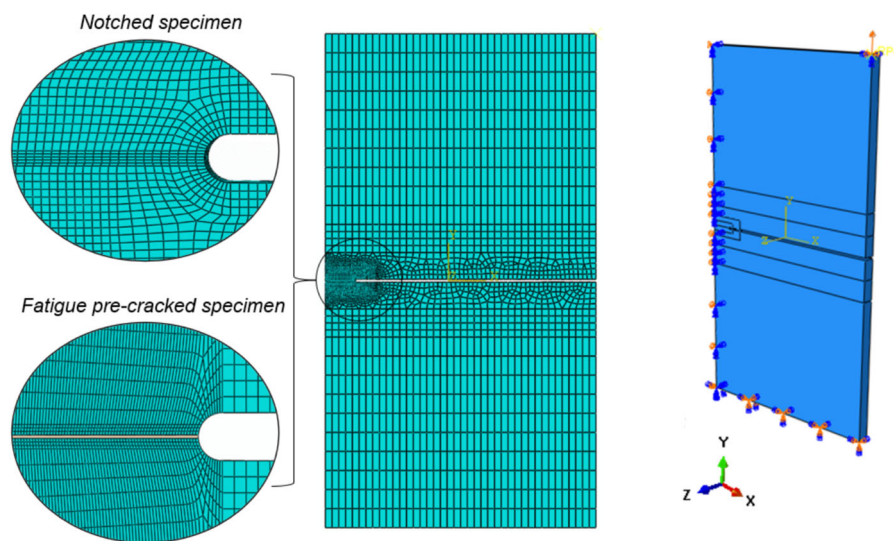


**Fig. 7** Mesh and boundary conditions used for 3D finite element model of notched and fatigue pre-cracked specimens

The damage evolution on the other hand defines the degradation behavior of the material once the initiation criterion has been met. The degradation of the material stiffness is associated with a scalar damage variable  $DI$ , defined as:

$$DI = \int \frac{d\varepsilon_p}{\varepsilon_f(\eta, \bar{\theta})} \leq 1 \quad (14)$$

where  $\varepsilon_f(\eta, \bar{\theta})$  is defined by Eq. 5 and the equivalent plastic strain ( $\varepsilon_p$ ) is given by:

$$\varepsilon_p = \int_0^t \sqrt{\frac{2}{3} \dot{\varepsilon}_{ij}^p \dot{\varepsilon}_{ij}^p} dt \quad (15)$$

When the index  $DI = 1$ , ductile degradation starts by growth and coalescence of voids until the final fracture.

### 3.2.2 Modelling of fracture

A common way to model crack growth in an elastic–plastic solid is the cohesive model, also known as traction–separation law. The concept was first proposed by Dugdale (1960); Barenblatt (1962) to describe the nonlinear fracture process in thin metal sheets. Dugdale (1960) assumes that within the plastic zone region, the stresses are constant and equal to the yield strength, while Barenblatt (1962) suggests a stress–strain softening relation that varies with the deformation. Hillerborg et al. (1976) were the first to apply the concept to model the cracking behavior of a concrete beam under bending. The model assumes that the material ahead of the crack tip is linear elastic until the stresses reach the tensile strength. The material starts then to soften and degrades but keeps its ability to transfer stresses across the discontinuity. The transferred stresses are a function of the crack opening ( $\delta$ ) and decrease linearly to zero at a critical opening ( $\delta_{co}$ ), beyond which the crack propagates. The fracture process is governed by the amount of energy absorbed per unit area in opening the crack ( $G_0$ ), expressed as:

$$G_0 = \int_0^{\delta_{co}} \sigma d\delta \quad (16)$$

The shape  $\sigma(\delta_{co})$  curve has a great influence on the material response. The linear softening function in Fig. 6 is the simplest and most common shape. However, different shapes were also proposed such

as trapezoidal law used by Tvergaard and Hutchinson (1992) to predict toughness in ductile fracture due to void growth and coalescence.

A standard approach to implement cohesive law in commercial finite element codes is the crack band model of Bažant and Oh (1983). The concept is frequently used to predict failure in quasi-brittle materials and assumes that a prescribed localization band appears inside each element when a crack develops. The relation between the crack opening displacement and fracture strain is expressed through  $\dot{\delta}_{CO} = \dot{\varepsilon}_p l_E$ , where  $l_E$  is the characteristic element length. The ductile damage model in Abaqus makes use of the crack band approach to reproduce the strain softening. After the onset of damage, the strain softening behavior of the material is characterized by a stress displacement response instead of a stress–strain. This requires introducing the characteristic length of the element ( $l_E$ ) to the equation, thus approximating the width of the crack surface i.e., crack band width. This concept allows to suppress the mesh sensitivity.

$$G_0 = \int_0^{\varepsilon_f} l_E \sigma d\varepsilon_p = G_0 = \int_0^{\delta_{co}} \sigma d\delta \quad (17)$$

Tvergaard and Hutchinson (1992) also made use of the cohesive law in finite element calculation to study ductile failure under small-scale yielding. For mode I plane strain, the traction–separation constitutive model is defined by two independent parameters, the work of separation ( $G_0$ ) and the tensile strength. The model introduces the cohesive length as a characteristic scale length and incorporates the effect of plastic strain in a modified traction separation relationship.

To account for the degradation of elastic stiffness, an internal scalar variable is defined and denoted herein by  $D$ . Physically, this internal damage variable represents the ratio of the area of the damaged material to the nominal cross-section area, therefore it takes values between 0 (for the undamaged material) and 1 (for the completely damaged material).  $D$  allows the transition of the elastic properties from the undamaged state to the damaged one according to  $(1-D) E$ . Its evolution according to ABAQUS (2012) User’s Manual is as follow:

$$\dot{D} = \frac{\sigma_u}{2G_0} \dot{\delta} \quad (18)$$

where  $\sigma_u$  is the value of the yield stress when  $DI = 1$  in Eq. 14. The value of  $D$  increases monotonously with the loading until reaching 1. Subsequently, the material loses its load-carrying capacity, and the element is removed from the mesh.

## 4 Results

### 4.1 Single $G_0$ value

The numerical model was initially fitted using a single value of fracture energy ( $G_0$ ) as material input in ABAQUS. The FE force–displacement curves match well with the experimental ones for the different ligament lengths of the same geometry. However, a deviation from the test curves was observed when the same  $G_0$  was used for the other notch radii. Therefore, different  $G_0$  values were used to fit the different notch sizes as shown in Table 2.

In the study of Pardoën et al. (2004), the works of separation and necking were split by applying a linear regression to the total work of fracture as a function of the thickness for several materials. The ratio  $G_0/G_n$  obtained for 1 mm thickness sheets showed that both contributions are in the same order of magnitude for most of the tested material. For instance, a  $G_0/G_n$  of 1.1 was reported for a stainless steel. According to Siegmund and Brocks (2000), the separation energy represents 0.5% to 12% of the total dissipation energy in a fully plastic condition depending on the specimen geometry, size, and crack extension. It can be observed from in Table 2.

Table 2 that both the work of necking,  $G_n$  and the separation energy,  $G_0$ , in CP1000HD are not constant and both increase continuously with the increase of the notch radius. The largest contribution to the total work of fracture comes from the work of necking, whereas the work of fracture represents less than 10% of the total work of fracture in all the geometries. It is worth mentioning that the variation in the work of fracture seems to influence the work of necking. The increase of  $G_0$  leaves room for progressive development of necking in the fracture process zone, leading to an increase in  $G_n$  as well. It results in an overall increase of the fracture toughness, in the measured  $w_e$ , as can be seen for DENT specimens with larger notch radius.

A similar trend was reported in previous studies. Frómota et al. (2020) investigated the sensitivity of the EWF parameters to the notch radius in several AHSS steel grades, QP (quenching and partitioning steel), DP (dual-phase), TBF (Transformation Induced Plasticity (TRIP)-aided Bainitic Ferritic) and CP (complex-phase). These steel grades showed different fracture resistance when tested with notched and fatigue precracked geometries. For instance, in CP  $w_e$  increased with the increase of the notch radius, meanwhile,  $w_p$  remained unaffected. On the other hand, for TBF and DP,  $w_e$  increased for notched specimens but  $w_p$  decreased for the fatigue ones. This seemed to affect smaller ligaments more than the larger ones. Similar for Q&P, but it seems to affect all ligaments. Similarly, Sunilkumar et al. (2021) explored the effect of notch radius on the fracture toughness in two automotive-grade dual phase steel (DP450) and IF (interstitial free) steel using EWF methodology. They came to the same conclusion that the sensitivity of the toughness to the notch radius is material dependent. The fracture energy sets the area under the softening curve. Any of the softening behavior represents an apparent change in the fracture energy, thus, the fracture toughness of the material. Accordingly, it is safe to say that the post-necking mechanical response of the material is also sensitive to the stress state.

CP1000HD belongs to this range of materials and that is the softening behavior after the maximum force in the force vs displacement curve cannot be described by a single fracture energy value. Therefore, to check the validity of this statement on this steel grade, a  $G_0$ - $\eta$  relationship was defined and implemented as a damage evolution function in Abaqus.

### 4.2 $G_0$ dependency on the stress triaxiality

The work of fracture dependency on the stress state has been addressed by a few authors over the last decades. The influence of triaxiality on the cohesive parameters was studied by Siegmund and Brocks (1999, 2000). It was found that the increase of the stress triaxiality results in a nonlinear increase of the cohesive strength and a decrease of the cohesive energy. Accordingly, the effect of specimen geometry and size, as well as the amount of crack extension have to be considered. Pineau and Pardoën (2007) stated that this dependency is described by an exponential

decay function for a range of triaxiality below 2–2.5. Above this range, the local fracture energy released ahead of the crack tip is independent of the triaxiality. Zhang et al. (2020) proved through experimental and numerical tests that the fracture energy is an exponentially decreasing function of the stress triaxiality.

In the present work, the triaxiality-dependent fracture energy function was implemented in ABAQUS by means of a VUSDFLD user subroutine. The quantitative relationship between these two quantities is approximated solely by FE calculations, as obtaining a correlation function experimentally requires time-consuming and extensive fracture tests and FE computations. The values of  $G_0$  in in Table 2.

Table 2 were used to roughly approximate the shape of the function in a triaxiality range between 0.5 and 3, then followed by an iterative method until the numerical force–displacement curve showed a good agreement with the experimental one. Figure 8 shows the variation of  $G_0$  as a function of  $\eta$  obtained from these FE computations. The local work of fracture at the crack tip decreases rapidly and monotonously from  $50 \text{ kJ/m}^2$  to  $10 \text{ kJ/m}^2$  for a range of  $\eta$  below 1.6. This range corresponds to low-constraint geometries, as notched specimens. With the increase of triaxiality above 1.6 in the high constraint geometry i.e., FPC,  $G_0$  reaches a plateau. The fracture behavior of the material in this range is described by constant  $G_0$  values.

Figure 9 displays the fit between the FE models and the experimental ones. Only 3 ligament lengths for each geometry were plotted herein. Overall, a

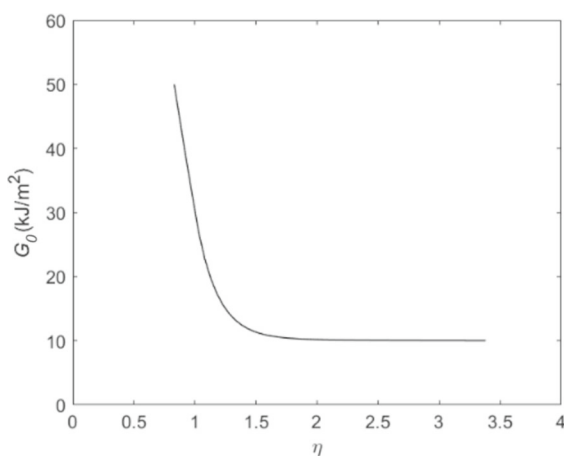


**Fig. 8** Correlation function between the local work of fracture  $G_0$  and the stress triaxiality  $\eta$  obtained from the FE computations

satisfactory agreement between the numerical and experimental data was obtained. The subroutine has a good predictive ability of the material degradation rate and strain softening after the onset of damage in different stress states. The crack initiation in each model was detected by the first element deleted and was marked by an asterisk (\*) on the force–displacement curves in Fig. 9. The stress constraints have a significant influence on the onset of the crack. In the high constraint geometry i.e., FPC, the crack initiates before the maximum tensile force. As the constraints ahead of the crack tip decrease with the increase of the notch radius, the onset of the crack is delayed. For the specimens with the lowest constraints i.e., NR250 and NR500, the onset of the fracture took place just before the softening and material degradation.

## 5 Discussion

Figure 10 shows the onset of the crack ( $DI = 1$ ) indicated by an asterisk (\*) on an exemplary force–displacement curve ( $l = 14 \text{ mm}$ ) for FPC, NR-150, NR-250 and NR-500. It can be seen that the initiation occurs at a different stage of deformation for each notch radius. The discontinuous lines A, B, C and D on the Figure correspond to the displacements at which damage is activated ( $DI = 1$ ) for the four geometries. It is evident that the crack initiation depends strongly on the notch size. As the notch radius decreases,  $DI$  reaches 1 at lower displacements. The initiation occurs largely before the peak load in FPC and NR150 (A and B), and around the maximum in NR250 (C). While, the crack initiates slightly before the final failure in NR500 (D). The distribution of the ductile failure parameters i.e.,  $\epsilon_p$ ,  $\eta$ ,  $\bar{\theta}$ ,  $D$  and  $DI$  along the ligament length at different moments of the crack propagation corresponding A–D are displayed in Fig. 11. An increase in the plastic strain can be seen amid the increase of the notch radius, meanwhile the triaxiality decreased and the Lode angle increased in the positive range. Consequently, the ultimate strain increased, as shown in .

Figure. 2 In all the geometries except FPC, the first damaged element  $DI = 1$  is at a certain distance from the crack front despite large  $\epsilon_p$ . This is due to the large stress triaxiality in the middle part of the specimen. It can be presumed that the nucleation and growth of

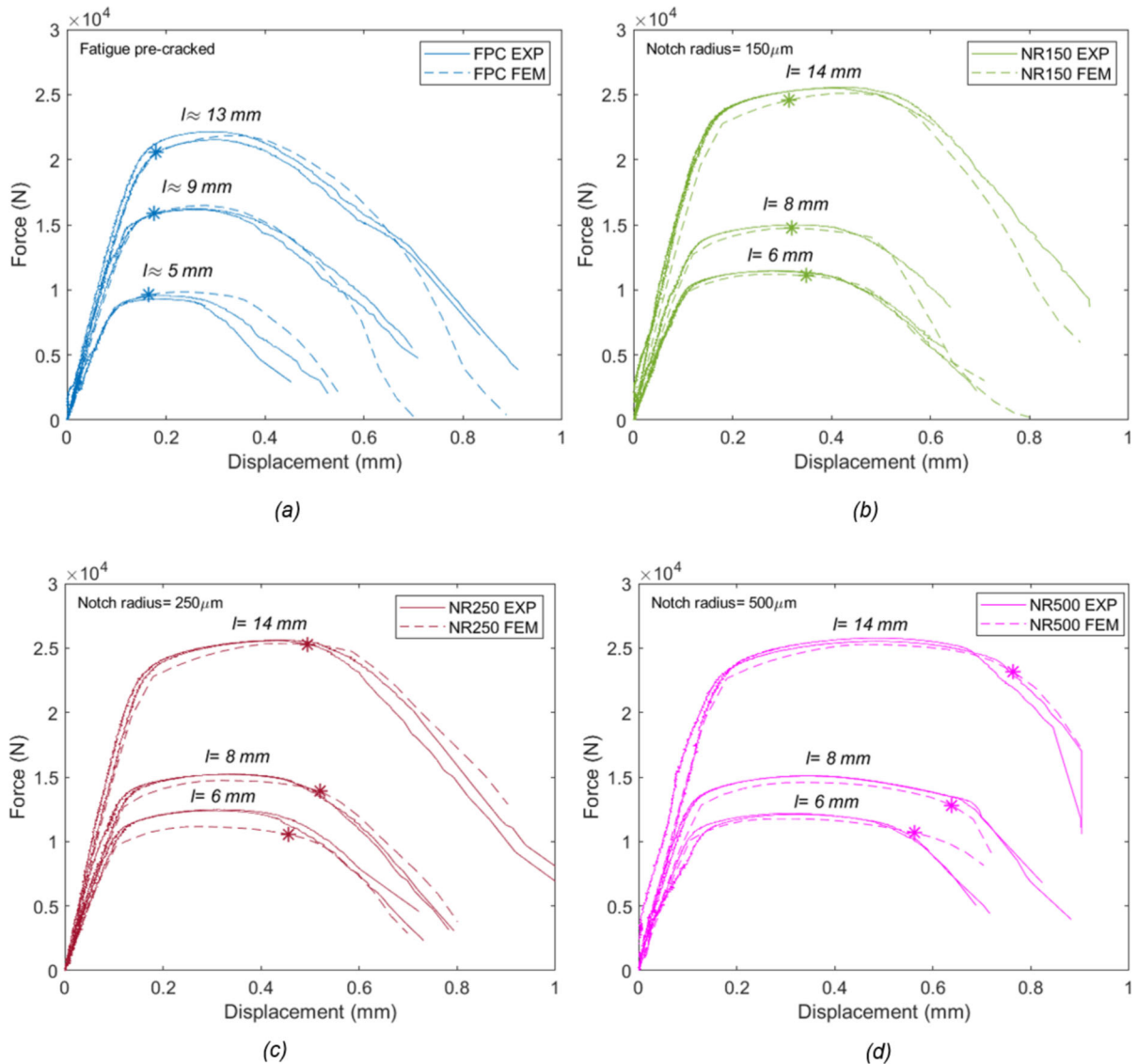
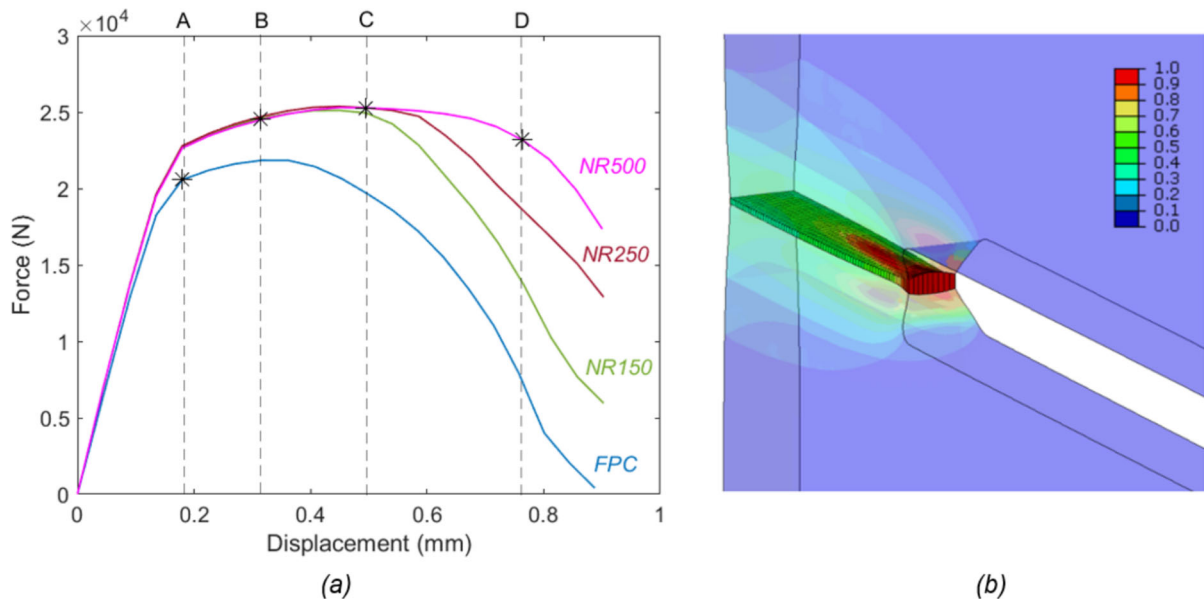


**Fig. 9** Experimental-numerical validation of the Force–displacement curves using the triaxiality-dependent fracture energy function as damage evolution law. **a** FPC; **b** NR150;

**c** NR250; **d** NR500. The onset of the crack propagation determined numerically is marked in the plot by \*

voids might have started inside the ligament zone and not at the notch root. One can also observe from Fig. 11 that the region of active damage  $0 < D < 1$  is restricted to a small area in front of the notch root and expands with the increase of the notch radius. The stress state close to the specimen edges is plane stress,

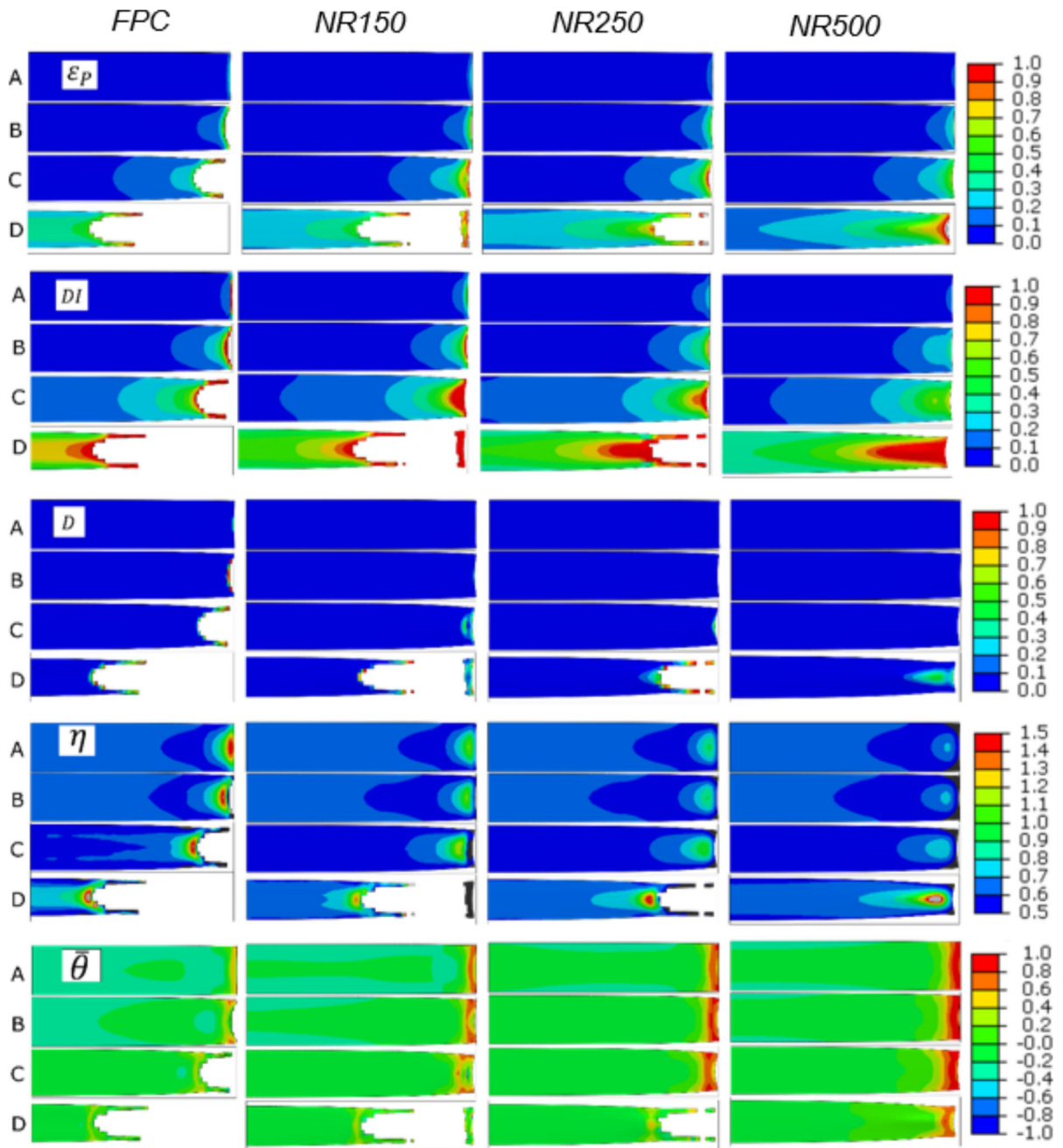
while plane strain prevails in the center. Consequently, the crack grows at different stress conditions through the specimen thickness and propagates faster in the center, leading to a curved crack front also known as “thumb nail”.



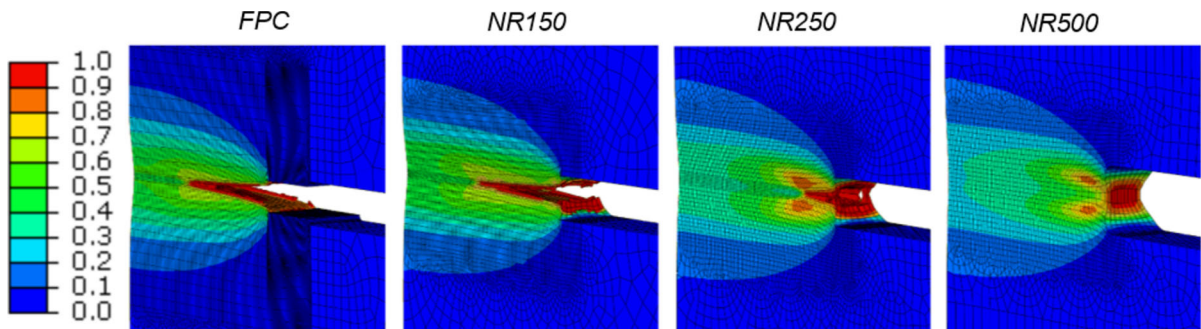
**Fig. 10** **a** Numerical Force–displacement response for the exemplary selected ligaments: ( $l \approx 13$  mm) for FPC and ( $l = 14$  mm) for NR150, NR250, NR500; **b** damage index ( $DI$ ) at failure plane for R500 at point D

Figure 12 displays the final failure of the four geometries using the proposed ductile damage model. According to the numerical computations, the low triaxiality in large notch radii specimens results in an increase of the fracture energy  $G_0$ . Furthermore, the larger  $\varepsilon_P$  and necking ability that these specimens

exhibit compared to fatigue precracked ones, lead to an increase of  $G_n$  as well. Nonetheless, the damage variable ( $DI$ ) reaches its maximum values at mid-thickness, in all geometries. As a result, the energy dissipated near the free edge is always larger than the center of the specimen.



**Fig. 11** Evolution of variables at failure plane at different deformation stages A, B, C and D as defined in Fig. 10, with  $\epsilon_p$  plastic energy,  $DI$  damage index,  $D$  damage variable,  $\eta$  stress triaxiality,  $\bar{\theta}$  normalized Lode angle



**Fig. 12** Contour plot of the damage index ( $DI$ ) at a displacement of 0.765 mm (point D of Fig. 10) for the largest ligament length and different notch radii after fracture

## 6 Conclusion

This paper addresses the softening behavior at the post-necking stress–strain curve of a high strength CP steel sheet by considering the evolution of  $G_0$  and  $G_n$  as a function of the stress triaxiality during crack initiation and propagation. The failure function was established numerically by means of a VUSDFLD user subroutine. Comparison of the numerically predicted force–displacement curves with the experimentally measured ones shows satisfactory results in terms of post-necking behavior for all four specimen types. This confirms the ability of the proposed failure function to successfully reproduce the softening of the material at different stress states. Then, the proposed approach can be used to address the fracture or damage modelling of thin-walled components or structures subjected to structural requirements.

The following conclusions can be drawn from the analysis of numerical models of CP1000HD with different notch radii:

- The softening behavior shown in the post-necking regime under different triaxiality conditions can be accurately estimated using an exponential decay function of the fracture energy ( $G_0$ ) and the stress triaxiality ( $\eta$ ).
- The local damage parameters ( $G_0$  and  $G_n$ ) are strongly dependent on the geometrical constraints, therefore the variability of the stress state should be considered in different constraint geometries.
- These two quantities are proportional, as  $G_0$  increases with  $\eta$ ,  $G_n$  increases too. However, this dependency is not linear.
- The sensitivity of the fracture energy  $G_0$  to the stress triaxiality  $\eta$  is significant between

approximately 0.7 and 1.5. Above this range,  $\eta$  seems to have no influence on  $G_0$ .

- The work of separation ( $G_0$ ) represents less than 10% of the essential work of fracture ( $w_e$ ), with the largest contribution coming from necking ( $G_n$ ).
- The increase of the notch radius results in a decrease of the stress triaxiality, but an increase of the normalized Lode angle in the positive range and the ultimate failure strain ( $\varepsilon_f$ ).
- The damage variable reaches its critical value ( $DI = 1$ ) at earlier deformation stage for low notch radius.

**Acknowledgements** I.T. is a fellow of Eurecat’s “Vicente López” PhD grant program. Open Access funding provided thanks to the CRUE-CSIC agreement with Springer.

**Author contributions** IT has written the original draft and performed the investigation. All authors have prepared the methodology of the manuscript. IT and PM have made the numerical model. PM, DF and DC have prepared the conceptualization, performed the validations, the reviewing and the editing of the Manuscript.

**Data availability** No datasets were generated or analysed during the current study.

### Declarations

**Conflict of interest** The authors have no conflicts of interest to declare that are relevant to the content of this article.

**Open Access** This article is licensed under a Creative Commons Attribution 4.0 International License, which permits use, sharing, adaptation, distribution and reproduction in any medium or format, as long as you give appropriate credit to the original author(s) and the source, provide a link to the Creative Commons licence, and indicate if changes were made. The images or other third party material in this article are included in the article’s Creative Commons licence, unless indicated

otherwise in a credit line to the material. If material is not included in the article's Creative Commons licence and your intended use is not permitted by statutory regulation or exceeds the permitted use, you will need to obtain permission directly from the copyright holder. To view a copy of this licence, visit <http://creativecommons.org/licenses/by/4.0/>.

## References

- ABAQUS 6.12 (2012) Analysis User's Manual Volume IV: Elements, Dassault Systèmes. <http://130.149.89.49:2080/v6.12>. Accessed 6 Jan 2020
- Algarni M, Bai Y, Choi Y (2015) A study of Inconel 718 dependency on stress triaxiality and Lode angle in plastic deformation and ductile fracture. *Eng Fract Mech* 147:140–157. <https://doi.org/10.1016/j.engfracmech.2015.08.007>
- Bai Y, Wierzbicki T (2008) A new model of metal plasticity and fracture with pressure and Lode dependence. *Int J Plast* 24(6):1071–1096. <https://doi.org/10.1016/j.ijplas.2007.09.004>
- Bai Y, Wierzbicki T (2009) Application of extended Mohr-Coulomb criterion to ductile fracture. *Int J Fract* 161(1):1–20. <https://doi.org/10.1007/s10704-009-9422-8>
- Bao Y, Wierzbicki T (2004) On fracture locus in the equivalent strain and stress triaxiality space. *Int J Mech Sci* 46(1):81–98. <https://doi.org/10.1016/j.ijmecsci.2004.02.006>
- Barenblatt GI (1962) The mathematical theory of equilibrium cracks in brittle fracture. *Adv Appl Mech*. [https://doi.org/10.1016/s0065-2156\(08\)70121-2](https://doi.org/10.1016/s0065-2156(08)70121-2)
- Barsoum I, Faleskog J (2007) Rupture mechanisms in combined tension and shear—micromechanics. *Int J Solids Struct* 44(17):5481–5498. <https://doi.org/10.1016/j.ijsolstr.2007.01.010>
- Barsoum I, J. Faleskog J, (2011) Micromechanical analysis on the influence of the Lode parameter on void growth and coalescence. *Int J Solids Struct* 48(6):925–938. <https://doi.org/10.1016/j.ijsolstr.2010.11.028>
- Bazant ZP, Oh BH (1983) Crack band theory for fracture of concrete. *Mat Et Constr* 16(3):155–177. <https://doi.org/10.1007/bf02486267>
- CEN workshop agreement CWA 17793 (2021) Test method for determination of the essential work of fracture of thin ductile metallic sheets.
- Cotterell BB, Reddel JK (1977) The essential work of plane stress ductile fracture. *Int J Fract* 13(3):267–277. <https://doi.org/10.1007/bf00040143>
- Dugdale DS (1960) Yielding of steel sheets containing slits. *J Mech Phys Solids* 8(2):100–104. [https://doi.org/10.1016/0022-5096\(60\)90013-2](https://doi.org/10.1016/0022-5096(60)90013-2)
- Dunand M, Mohr D (2011) On the predictive capabilities of the shear modified Gurson and the modified Mohr-Coulomb fracture models over a wide range of stress triaxialities and Lode angles. *J Mech Phys Solids* 59(7):1374–1394. <https://doi.org/10.1016/j.jmps.2011.04.006>
- Frómata D et al (2017) Assessing edge cracking resistance in AHSS automotive parts by the essential work of fracture methodology. *J Phys Conf Ser*. <https://doi.org/10.1088/1742-6596/896/1/012102>
- Frómata D et al (2019a) On the correlation between fracture toughness and crash resistance of advanced high strength steels. *Eng Fract Mech* 205:319–332. <https://doi.org/10.1016/j.engfracmech.2018.10.005>
- Frómata D, Lara A, Casas B, Casellas D (2019b) Fracture toughness measurements to understand local ductility of advanced high strength steels. *IOP Conf Ser Mater Sci Eng* 651(1):012071. <https://doi.org/10.1088/1757-899x/651/1/012071>
- Frómata D et al (2020) Identification of fracture toughness parameters to understand the fracture resistance of advanced high strength sheet steels. *Eng Fract Mech* 229:106949. <https://doi.org/10.1016/j.engfracmech.2020.106949>
- Gao X, Kim J (2006) Modeling of ductile fracture: significance of void coalescence. *Int J Solids Struct* 43(20):6277–6293. <https://doi.org/10.1016/j.ijsolstr.2005.08.008>
- Gao X, Wang T, Kim J (2005) On ductile fracture initiation toughness: effects of void volume fraction, void shape and void distribution. *Int J Solids Struct* 42(18–19):5097–5117. <https://doi.org/10.1016/j.ijsolstr.2005.02.028>
- Gao X, Zhang G, Roe CP (2009) A study on the effect of the stress state on ductile fracture. *Int J Damage Mech* 19(1):75–94. <https://doi.org/10.1177/1056789509101917>
- Garrison WM, Moody NR (1987) Ductile fracture. *J Phys Chem Solids* 48(11):1035–1074. [https://doi.org/10.1016/0022-3697\(87\)90118-1](https://doi.org/10.1016/0022-3697(87)90118-1)
- Hancock JW, Brown DK (1983) On the role of strain and stress state in ductile failure. *J Mech Phys Solids* 31(1):1–24. [https://doi.org/10.1016/0022-5096\(83\)90017-0](https://doi.org/10.1016/0022-5096(83)90017-0)
- Hancock JW, Mackenzie A (1976) On the mechanisms of ductile failure in high-strength steels subjected to multi-axial stress-states. *J Mech Phys Solids* 24(2–3):147–160. [https://doi.org/10.1016/0022-5096\(76\)90024-7](https://doi.org/10.1016/0022-5096(76)90024-7)
- Hilditch T, De Souza T, Hodgson P (2015) Properties and automotive applications of advanced high-strength steels (AHSS). Elsevier eBooks, Amsterdam, pp 9–28
- Hillerborg A, Modéer M, Petersson PE (1976) Analysis of crack formation and crack growth in concrete by means of fracture mechanics and finite elements. *Cem Concr Res* 6(6):773–781. [https://doi.org/10.1016/0008-8846\(76\)90007-7](https://doi.org/10.1016/0008-8846(76)90007-7)
- Hosford WF, Atkins AG (1990) On fracture toughness in tearing of sheet metal. *J Mater Shap Technol* 8(2):107–110. <https://doi.org/10.1007/bf02833622>
- Kaufman JG (2001) Fracture resistance of aluminum alloys: notch toughness, tear resistance, and fracture toughness. *ASM Int*. <https://doi.org/10.31399/asm.hb.v02b.a0006457>
- Kim J, Gao X, Srivatsan TS (2004) Modeling of void growth in ductile solids: effects of stress triaxiality and initial porosity. *Eng Fract Mech* 71(3):379–400. [https://doi.org/10.1016/s0013-7944\(03\)00114-0](https://doi.org/10.1016/s0013-7944(03)00114-0)
- Koplik J, Needleman A (1988) Void growth and coalescence in porous plastic solids. *Int J Solids Struct* 24(8):835–853. [https://doi.org/10.1016/0020-7683\(88\)90051-0](https://doi.org/10.1016/0020-7683(88)90051-0)
- Li Y, Luo M, Gerlach JC, Wierzbicki T (2010) Prediction of shear-induced fracture in sheet metal forming. *J Mater Process Technol* 210(14):1858–1869. <https://doi.org/10.1016/j.jmatprotec.2010.06.021>

- Ma YS, Sun DZ, Andrieux F et al (2017) Influences of initial porosity, stress triaxiality and Lode parameter on plastic deformation and ductile fracture. *Acta Mech Solida Sin* 30:493–506. <https://doi.org/10.1016/j.camss.2017.10.002>
- Mai Y (1993) On the plane-stress essential fracture work in plastic failure of ductile materials. *Int J Mech Sci* 35(12):995–1005. [https://doi.org/10.1016/0020-7403\(93\)90051-u](https://doi.org/10.1016/0020-7403(93)90051-u)
- Mai Y, Powell PC (1991) Essential work of fracture and J-integral measurements for ductile polymers. *J Polym Sci Part B* 29(7):785–793. <https://doi.org/10.1002/polb.1991.090290702>
- Marth S, Häggblad H, Oldenburg M, Östlund R (2016) Post necking characterisation for sheet metal materials using full field measurement. *J Mater Process Technol* 238:315–324. <https://doi.org/10.1016/j.jmatprotec.2016.07.036>
- McClintock FA (1968) A criterion for ductile fracture by the growth of holes. *J Appl Mech* 35(2):363–371. <https://doi.org/10.1115/1.3601204>
- Omiya M et al (2022) Influence of strength and notch shape on crack initiation and propagation behavior of advanced high strength steel sheets. *Eng Fract Mech* 271:108573. <https://doi.org/10.1016/j.engfracmech.2022.108573>
- Pardoent T, Hutchinson JW (2000) An extended model for void growth and coalescence. *J Mech Phys Solids* 48(12):2467–2512. [https://doi.org/10.1016/s0022-5096\(00\)00019-3](https://doi.org/10.1016/s0022-5096(00)00019-3)
- Pardoent T, Hachez F, Marchioni B, Blyth PH, Atkins AG (2004) Mode I fracture of sheet metal. *J Mech Phys Solids* 52(2):423–452. [https://doi.org/10.1016/s0022-5096\(03\)00087-5](https://doi.org/10.1016/s0022-5096(03)00087-5)
- Pineau A, Pardoent T (2007) Failure mechanisms of metals. *Comprehensive structural integrity encyclopedia*. Elsevier, Amsterdam, pp 687–783
- Pluvinage G (2001) Notch effects in fatigue and fracture. Notch effects in fatigue and fracture. Springer, Dordrecht, pp 1–22
- Pluvinage G, Gilgert J (2003) Fracture emanating from stress concentrators in materials: links with classical fracture mechanics. *Materiali in Tehnologije* 37(3/4):117–122
- Rice JR, Tracey DM (1969) On the ductile enlargement of voids in triaxial stress fields. *J Mech Phys Solids* 17(3):201–217. [https://doi.org/10.1016/0022-5096\(69\)90033-7](https://doi.org/10.1016/0022-5096(69)90033-7)
- Sandin O, Jonsén P, Frómeta D, Casellas D (2021) Stating failure modelling limitations of high strength sheets: implications to sheet metal forming. *Materials* 14(24):7821. <https://doi.org/10.3390/ma14247821>
- Siegmund T, Brocks W (1999) Prediction of the work of separation and implications to modeling. *Int J Fract* 99:97–116. <https://doi.org/10.1023/A:1018300226682>
- Siegmund T, Brocks W (2000) A numerical study on the correlation between the work of separation and the dissipation rate in ductile fracture. *Eng Fract Mech* 67(2):139–154. [https://doi.org/10.1016/s0013-7944\(00\)00054-0](https://doi.org/10.1016/s0013-7944(00)00054-0)
- Srivastava A, Needleman A (2013) Void growth versus void collapse in a creeping single crystal. *J Mech Phys Solids* 61(5):1169–1184. <https://doi.org/10.1016/j.jmps.2013.01.006>
- Stiebler K, Kunze H, El-Magd E (1991) Description of the flow behaviour of a high strength austenitic steel under biaxial loading by a constitutive equation. *Nucl Eng des* 127(1):85–93. [https://doi.org/10.1016/0029-5493\(91\)90041-f](https://doi.org/10.1016/0029-5493(91)90041-f)
- Sunilkumar MR et al (2021) Fracture toughness examination of dual-phase and interstitial free steel using essential work of fracture method. *Fatigue Fract Eng Mater Struct* 44(12):3272–3288. <https://doi.org/10.1111/ffe.13555>
- Tvergaard V, Hutchinson JW (1992) The relation between crack growth resistance and fracture process parameters in elastic-plastic solids. *J Mech Phys Solids* 40(6):1377–1397. [https://doi.org/10.1016/0022-5096\(92\)90020-3](https://doi.org/10.1016/0022-5096(92)90020-3)
- Van Stone RH, Cox TB, Low JR, Psioda JA (1985) Microstructural aspects of fracture by dimpled rupture. *Int Metals Rev* 30(1):157–180. <https://doi.org/10.1179/imtr.1985.30.1.157>
- Vratnica M, Pluvinage G, Jodin P, Cvijović Z, Rakin M, Burzić Z (2010) Influence of notch radius and microstructure on the fracture behavior of Al–Zn–Mg–Cu alloys of different purity. *Mater Eng* 31(4):1790–1798. <https://doi.org/10.1016/j.matdes.2009.11.018>
- Wierzbicki T, Bao Y, Lee YW, Bai Y (2005) Calibration and evaluation of seven fracture models. *Int J Mech Sci* 47(4–5):719–743. <https://doi.org/10.1016/j.ijmesci.2005.03.003>
- Xue L (2007) Damage accumulation and fracture initiation in uncracked ductile solids subject to triaxial loading. *Int J Solids Struct* 44(16):5163–5181. <https://doi.org/10.1016/j.ijsolstr.2006.12.026>
- Yu QM (2015) Influence of the stress state on void nucleation and subsequent growth around inclusion in ductile material. *Int J Fract* 193:43–57. <https://doi.org/10.1007/s10704-015-0016-3>
- Zhang KS, Bai JB, François D (2001) Numerical analysis of the influence of the lode parameter on void growth. *Int J Solids Struct* 38(32–33):5847–5856. [https://doi.org/10.1016/s0020-7683\(00\)00391-7](https://doi.org/10.1016/s0020-7683(00)00391-7)
- Zhang T, Yuan H, Yang S (2020) Fracture energy and tensile strength depending on stress triaxiality along a running crack front in three-dimensional cohesive modelling. *Eng Fract Mech* 227:106919. <https://doi.org/10.1016/j.engfracmech.2020.106919>
- Zhu Y, Engelhardt MD, Kiran R (2018) Combined effects of triaxiality, lode parameter and shear stress on void growth and coalescence. *Eng Fract Mech* 199:410–437. <https://doi.org/10.1016/j.engfracmech.2018.06.008>

**Publisher's Note** Springer Nature remains neutral with regard to jurisdictional claims in published maps and institutional affiliations.